Equilibrium climate sensitivity controls uncertainty in regional climate change over the 21st century

Cristian Proistosescu[a,b,c,1], **David S. Battisti**[d], **Kyle C. Armour**[d,e], **and Gerard H. Roe**[f]

[a]Department of Atmospheric Sciences, University of Illinois Urbana-Champaign, Urbana, IL; [b]Department of Geology, University of Illinois Urbana-Champaign, Urbana, IL; [c]formerly at Joint Institute for the Study of the Atmosphere and Ocean, University of Washington, Seattle, WA; [d]Department of Atmospheric Sciences, University of Washington, Seattle, WA; [e]School of Oceanography, University of Washington, Seattle, WA; [f]Department of Earth and Space Sciences, University of Washington, Seattle, WA

This manuscript was compiled on April 13, 2020

Improved projections of local temperature change over the 21st century are essential for evaluating impacts and setting policy targets (1, 2). Uncertainty in these projections is due to two approximately equal factors: uncertainty in greenhouse gas emissions, and uncertainty in the response of climate to those emissions (3). For the latter, it is well known that climate models all have a similar global pattern of warming (4). Here, we show that differences among projections of warming also share a common pattern of variability. Specifically, the leading empirical orthogonal function (EOF) of inter-model differences strongly resembles the ensemble-mean response itself. This pattern explains 60% of the total variance in projected regional warming, with higher fractions of variance explained over tropics and mid-latitudes. When projected onto the model residuals, it is strongly correlated ($r^2 = 0.9$) with Equilibrium Climate Sensitivity (ECS), and more-weakly correlated with the Transient Climate Response (TCR, $r^2 = 0.6$). We show how this strong correlation between equilibrium global warming and transient regional warming uncertainty arises due to the large scales over which the atmosphere mixes energetic perturbations. The dominant source of variance in both ECS and 21st-century warming are low-latitude feedbacks, whereas TCR is more sensitive to uncertainties in CO_2 radiative forcing and ocean heat uptake. The results imply that throughout the tropics and mid-latitudes, and especially over land, most of the uncertainty in local temperature projections is due to model differences in tropical cloud feedbacks.

climate sensitivity | local climate change | temperature | moisture transport

We do not live in the global mean. Both impacts and perceptions of climate change depend on the patterns of regional climatic change, and how these patterns interact with population density (1). Similarly, policies designed to limit the effects of climate change are often decided by considering targets for regional warming (2). While the overall pattern of regional warming has long been known (5, 6), little progress has been made in reducing the significant uncertainty in the magnitude of regional climate change (4). Uncertainties in the magnitude of regional warming expected by the end of 21st century come in roughly equal amounts from uncertainties in emission pathways, and uncertainties in the physical response of the system (3, 7). In order to better forecast, mitigate, and adapt to the impacts of climate change, it is crucial to understand and reduce uncertainties in the regional temperature response to greenhouse gas emissions.

Projections of regional 21st century temperature change have been made with ensembles of numerical climate models (8). The ensemble-mean pattern of warming is characterized by amplified warming over land and high latitudes (Fig. 1A). This pattern of both land and polar amplification arises through the combined effects of less-negative high-latitude radiative feedbacks (9, 10) and atmospheric energy-transport tendencies, the latter of which act to transport moist-static energy downgradient both zonally (11) and meridionally (12). The ensemble spread in regional warming exhibits a similar pattern (Fig. 1B). The ensemble spread is largest where the ensemble-mean warming is largest, with the notable exception of the Southern Ocean and the sub-polar North Atlantic Ocean .

Here we show how these uncertainties in regional 21st century warming relate to better-quantified uncertainties in metrics of global temperature response, namely equilibrium climate sensitivity (ECS) and the transient climate response (TCR). We then illustrate how this pattern of uncertainty is driven by the same physical mechanisms that give rise to the ensemble-mean warming pattern – radiative feedbacks and atmospheric and oceanic heat transport. Finally, we explain why 21st century warming is better predicted by ECS than by TCR (13).

Patterns of Regional Uncertainty

We focus on regional temperature changes in an ensemble of 25 General Circulation Models (GCMs) from phase five of the Coupled Model Intercomparison Project, (CMIP5 (14), Table S1). These model were the basis for climate-change projections in the fifth assessment report of the Intergovernmental Panel on Climate Change (IPCC AR5 (8)). We define 21st-century

Significance Statement

Societal impacts of anthropogenic global warming are determined by local climatic changes in temperature and precipitation. Uncertainties in the physical climate response to carbon emissions accounts for approximately as much of the spread in predictions of future warming as the uncertainty in socio-economic scenarios. We characterize the uncertainty patterns for end-of-century temperature response, and show that they are tightly related to uncertainties in Earth's long-term climate sensitivity. Our results show that constraining equilibrium climate sensitivity, such as from observational or palaeoclimate records, could lead to improved predictions of near-term regional temperature changes in the tropics and mid-latitudes, especially over land. In terms of processes, the largest improvement in regional temperature projections will be gained by reducing uncertainty in subtropical cloud feedbacks.

author contributions

The authors declare no conflict of interest

[1]To whom correspondence should be addressed. E-mail: cristi@illinois.edu

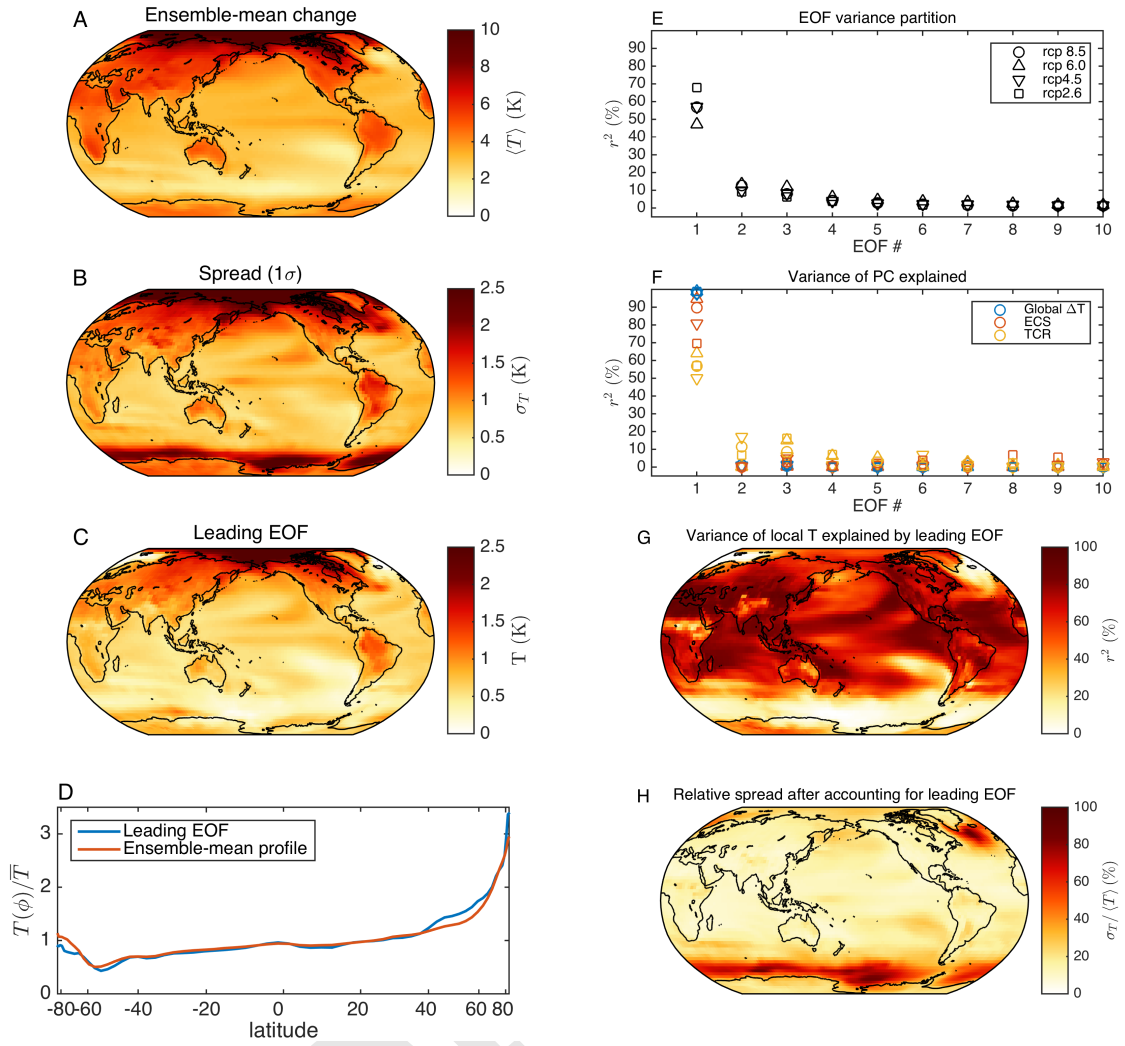

Fig. 1. Temperature response patterns and their uncertainty. (A) Ensemble-mean warming pattern over the twentieth century under RCP 8.5, defined as the difference between 2080-2099 averages minus 1980-1999 averages. (B) Ensemble spread of local temperature changes (1σ) around the ensemble mean. (C) Leading EOF of the spread in temperature change, computed by projecting the first principal component onto the spread. (D) Zonal-mean profiles of the leading EOF (blue) and the ensemble-mean temperature change (red). Both profiles are normalized to unit global-mean change. (E) Percentage of variance partitioned into each EOF. (F) Coefficient of determination: percentage of the variance of each principal component that can be explained by the spread in global-mean temperature, Equilibrium Climate Sensitivity (ECS), and Transient Climate Response (TCR). (G) Variance of local temperature change explained by the principal of the leading EOF. (H) Coefficient of variation: relative spread after taking out the contribution of the leading EOF.

temperature change as the difference between averages over years 1980-2000 in historical simulations and 2080-2100 in simulations using representative concentration pathways (RCPs, (15)). To maximize the signal-to-noise ratio of forced response to natural variability, we primarily use the high-emissions RCP8.5 scenario leading to 8.5 W/m^2 of radiative forcing by the end of the century (Fig. 1), although the main results hold across scenarios (Figs. S1-S3).

The spread in multi-model projections can be analyzed using empirical orthogonal functions (EOFs)*, which are a way to partition the ensemble spread in temperature changes into a basis of fixed patterns (the EOFs) and their associated principal components that describes how much the spread of a given model projects onto a given EOF. An analysis of the inter-model spread of 21st-century temperature changes reveals a leading EOF of model-spread that is very similar to the ensemble-mean pattern (Fig. 1C,D). Across scenarios, only the leading EOF is well separated and contains 59% of the total variance in the RCP-8.5 ensemble spread (Fig. 1E).

Across models, the magnitude of the dominant EOF pattern is highly coherent with a models' global-mean temperature change and ECS (Fig. 1F). For RCP 8.5, these squared correlations are $r^2 = 98\%$ and $r^2 = 90\%$, respectively. The first EOF explains 60% of global variance, however it explains much higher amounts of variance over large parts of the world, with values of r^2 in the 70% to 90% range over most of the tropics, mid-latitudes, and land (Fig. 1G). Of note, the coherence with TCR is substantially less ($r^2 = 60\%$), consistent with recent results suggesting ECS is a better predictor of 21st century temperature changes than TCR (13). Seasonal anomalies show similar results in terms of uncertainty being dominated by a single EOF, with a pattern similar to the ensemble mean, and a high correlation with ECS (Figs. S4-S7).

*Often known as Principal Component Analysis (PCA) in other fields of science.

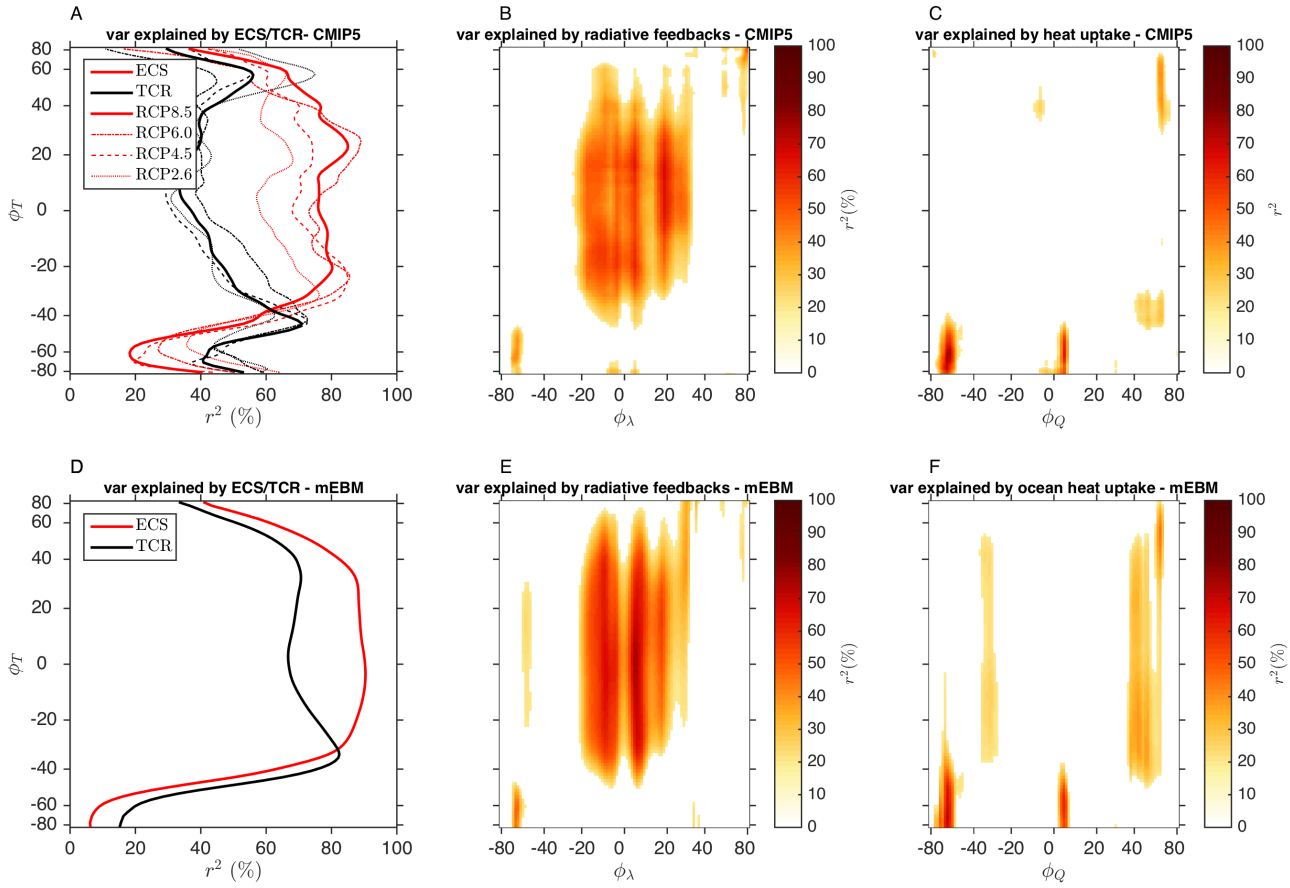

Fig. 2. Drivers of Uncertainty. (A) Percentage of the variance of zonal-mean temperature 21st century temperature change that can be explained by ECS (red) and TCR (black), across four RCP scenarios. (B) r^2: percentage of variance of the zonal-mean temperature change in RCP8.5 simulations at each latitude ϕ_T that can be explained by the variance in radiative feedacks, λ, at latitude ϕ_λ. Only values above a 95% confidence interval are shown. (C) same as (B) but for variance in CMIP5 temperature change explained by variance in ocean heat uptake. (D-F) same as (A-C) but for a moist energy balance model (MEBM, see methods).

The relative spread after accounting for the leading EOF is negligible over much of the Earth (Fig. 1H). Over most of the continents, the spread is in the range of 10-15% of the ensemble-mean response, with slightly higher values on the order of 30% over equatorial Africa and parts of South America. The regions where the leading EOF does not account for a significant part of the inter-model spread are regions of significant ocean heat uptake. The correlation of the dominant's EOF projection with a model's ECS and the similarity between its pattern and the ensemble mean implies that a majority of the model spread in future projections can be captured by scaling of the ensemble-mean pattern by the spread in ECS. The fact that within a single model the pattern of warming scales with global-mean temperature has long been used to infill projections between the standard scenarios (16–19). These results suggest that the same pattern scaling applies across models. Furthermore, the high correlation between the leading EOF and ECS implies that reducing uncertainty in ECS would significantly reduce uncertainty in regional temperature projections.

What physical mechanism drive uncertainty?

We can simplify the problem by adopting a zonal-mean view. Indeed, the correlation structure of ECS with zonal-mean temperature changes (Fig. 2A) is similar to that with local temperature. Across RCP scenarios the squared correlation coefficient r^2 between ECS and zonal-mean 21st century warming is high over low- and mid-latitudes and decreases substantially for high-latitudes, especially over the Southern Ocean. The correlation is lower for RCP4.5 and RCP2.6, likely because the forced response is smaller in these scenarios, and natural variability contributes more relative uncertainty.

The ensemble spread in temperature changes can be traced to ensemble spread in top-of-atmosphere (TOA) radiative feedbacks, ocean heat uptake, and radiative forcing (20). We take a more detailed look at this partition for 21st century warming in RCP8.5, by analyzing the squared correlation of zonal-mean temperature with radiative feedbacks and ocean heat uptake (see methods). Spread in local radiative forcing is not available or readily computable for CMIP5 historical and RCP simulations, but is expected to explain a small fraction of the variance (Fig. S8). The primary driver of uncertainty in low- and mid-latitude ($\sim 45°$S$-60°$N) 21st century warming is the large uncertainty in tropical and subtropical feedbacks ($\sim 20°$S$-30°$N) (Fig. 2B). In contrast, uncertainty over the Southern Ocean is driven primarily by local radiative feedbacks and ocean heat uptake (Fig. 2B,C).

The strong correlation of regional warming with ECS arises because the same low-latitude feedbacks that control uncertainty in regional temperature changes over a large part of the Earth also control uncertainty in ECS (21). The strong

correlation of Southern Ocean temperature with both TCR and ocean heat uptake suggests that TCR may also be more correlated to the spread in heat uptake. This would explain why TCR is more-weakly correlated with low- and mid-latitude temperature changes where the spread is controlled almost exclusively by radiative feedbacks.

The dominance of a single pattern of uncertainty, and thus the high correlation of local temperatures to global metrics of temperature change, is due to the large (meridional and zonal) mixing scales in the atmosphere. The relative contribution of low-latitude radiative feedback uncertainty from a given latitude, ϕ_λ, is approximately the same for temperature spread at any point in the low- and mid-latitudes (as evidenced by the strong self-similarity of r^2 as a function of latitude ϕ_T in Fig 2B).

A model for mixing scales

In order to understand what sets this partition of uncertainty between different physical processes at different latitudes, we need to understand how the atmosphere responds to perturbations in local feedbacks, ocean heat uptake, and radiative forcing. Zonal-mean energy budget anomalies can be decomposed into TOA radiative forcing R_f, surface ocean heat uptake Q, horizontal atmospheric heat-flux divergence $\nabla \cdot \mathbf{H}$, and a radiative response at the TOA that is assumed to be linearly proportional to temperature perturbations $R_T = \lambda \cdot T$:

$$0 = R_f(\phi) + Q(\phi) - \nabla_\phi H(\phi) - \lambda(\phi) \cdot T(\phi), \qquad [1]$$

where ϕ denotes latitude, and ∇_ϕ denotes the meridional gradient in spherical coordinates. For the remainder of the section, we will drop the ϕ notation, with the understanding that terms represent zonal means.

In order to model the meridional mixing scales, we need a dynamical rule for atmospheric heat transport, and we approximate atmospheric heat transport as governed by down-gradient diffusion of near-surface moist static energy (MSE) h, following several recent studies (12, 20, 22–25),

$$\nabla_\phi H = D \nabla_\phi^2 h, \qquad [2]$$

with $h = c_p T + L_\nu q$, where c_p is the specific heat at constant pressure, L_ν is the latent heat of vaporization, q is change in specific humidity, and D is a constant diffusion coefficient. This simple moist energy balance model (MEBM) has been shown to reproduce the CMIP5 ensemble spread in both temperature (20) and meridional heat-transport anomalies (12). Crucially, the MEBM allows us to directly attribute the spread in the temperature response to the spread in the different forcing terms in Eqn. 1. We find the MEBM is able to reproduce the correlation structure and mixing scales of zonal-mean temperature with ECS, TCR (Fig. 2D), radiative feedbacks (Fig. 2E), and ocean heat uptake (Fig. 2F).

Response patterns. Using the dynamical rule for heat transport allows us to compute the response function to a local energetic perturbation, in a way that cannot be done with a statistical decomposition of the energy budget in GCMs. Let $\langle T \rangle$ be the ensemble-mean response to an ensemble-mean abrupt CO_2 forcing, $\langle R_f \rangle$, with ensemble-mean radiative feedbacks, $\langle \lambda \rangle$, and heat uptake $\langle Q \rangle$. An individual model's response can be described as a perturbation δT from the ensemble mean,

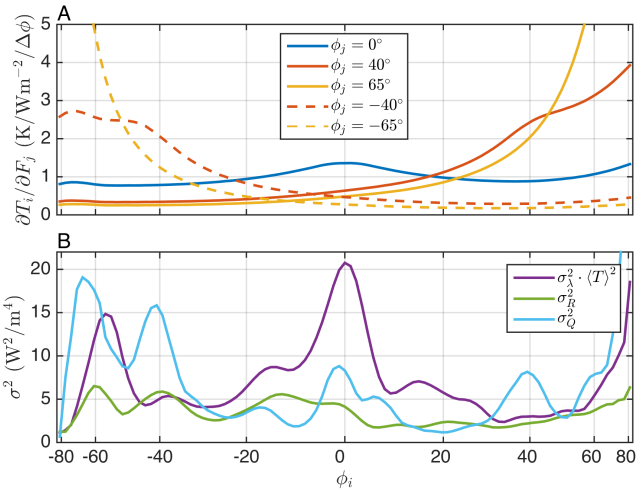

Fig. 3. Moist Energy Balance Model (A) Response function, $\partial T(\phi_i)/\partial F(\phi_j)$, showing how a prescribed increased uncertainty in forcing δF at five representative latitudes ϕ_j leads to increased uncertainty in temperature across all latitudes, ϕ_i. (B) The variance in forcing terms, δF in Eqn. 3, calculated from the ensemble of CMIP5 models (20).

which can be tied to that model's perturbations from the ensemble mean in radiative forcing, δR_f, heat uptake, δQ , and feedbacks, $\delta\lambda$:

$$\langle \lambda \rangle \, \delta T - D \nabla_\phi^2 \delta h = \underbrace{\delta R_f + \delta Q + \delta\lambda \, \langle T \rangle}_{\delta F}, \qquad [3]$$

where second-order perturbations have been neglected, and each term is understood to represent zonal-mean values at a latitude ϕ.

The response function $\partial T(\phi_i)/\partial F(\phi_j)$ for a perturbation in any of the forcing terms, F, on the right-hand side of Eqn. 3 is depicted in Fig. 3A for perturbations imposed at a set of 5 representative latitudes (Methods). A perturbation concentrated on the equator leads to a relatively uniform response across all latitudes. However, a perturbation concentrated in polar regions leads to a response that is strongly polar amplified with relatively little influence on the tropics. The response function of the MEBM is supported by the response of full GCMs to narrow-band perturbations in either ocean heat uptake (24) or CO_2 forcing (10).

To understand this response structure we need to consider how the system closes its energy budget. If a local perturbation δF is applied (right-hand side of Eqn. 3), the system responds by radiatively damping to space and by meridionaly exporting MSE (left-hand side terms in Eqn. 3). The meridional export of MSE, h, is accomplished through a sensible heat term $c_p T$, and a latent heat term $L_\nu q$. Since q scales exponentially with temperature following Clausius-Clapeyron, the relative importance of latent to sensible heat will also increase dramatically with temperature.

In high latitudes, the lower climatological temperature requires that the lion's share of the energy export has to be accomplished via transport of sensible heat. Consequently, for a constant diffusion coefficient of MSE, the effective coefficient for diffusion of temperature is four times lower at the poles compared to the equator (22). Thus, the efficiency of energy export (meridional energy exported per degree of local temperature change) – is weaker in the high latitudes. Radiative

feedbacks are also less negative in the high latitudes. The lower efficiency of both TOA radiative damping and meridional heat export results in a large and zonally confined high-latitude temperature response being required to balance high-latitude forcing (12) (Fig. 3A).

In contrast, the larger climatological temperatures in the low-latitudes results in more efficient energy export through meridional fluxes of latent heat. Thus, a perturbation δF in low-latitudes does not have to be balanced by a large local increase in temperature. Instead the energy is exported through meridional moisture transport, leading to a smaller but near global increase in temperature and radiative damping.

The decrease of both radiative damping and meridional heat transport efficiency with increasing latitude can help explain the patterns of both the ensemble-mean response and the ensemble spread. The large high-latitude response required to balance local forcing leads to polar amplification – a basic feature of the climate response to CO_2 forcing. Land amplification, the other ubiquitous feature of the response to radiative forcing, can also be explained by the tendency of atmospheric heat transport to minimize gradients in zonal near-surface MSE (11): since the relative humidity is lower over land than over oceans, equal changes in MSE requires more warming over land than over ocean, because a greater fraction of the change in MSE has to be accomplished through changes in sensible heat content.

Patterns of uncertainty. The ensemble spread in zonal-mean temperature response T at a given latitude ϕ can be decomposed into contributions from the ensemble spread in feedbacks, heat uptake, and radiative forcing at every latitude ϕ_j,

$$\sigma_T^2 = \sum_j \left(\frac{\partial T}{\partial F_j} \right)^2 \left(\sigma_{Rf_j}^2 + \sigma_{Q_j}^2 + \sigma_{\lambda_j}^2 \langle T_j \rangle^2 \right), \quad [4]$$

where we have made the assumption that perturbations in each of the three forcing terms on the right-hand side are independent of each other, and between latitudes. The variance of the CMIP5 ensemble spread in radiative forcing, heat uptake, and radiative feedbacks are shown in Fig. 3B. The highest source of inter-model spread comes from the spread in low-latitude feedbacks and Southern Ocean heat uptake, with some additional variance in high-latitude feedbacks, and heat uptake in the northern mid-latitudes. This combination of the structure of the response function (Fig. 3A) and process uncertainty (Fig. 3B) explains the partition of uncertainty observed in Fig. 2.

High-latitude warming is most sensitive to local feedbacks, forcing, and heat-uptake (10, 25), and thus uncertainty in high-latitude warming is dominated by uncertainty in these local terms (20). Consequently, high-latitude warming in poorly predicted predicted by ECS, which is dominated by low-latitude processes. Outside the high latitudes, the response is more uniform, and warming uncertainty is dominated by the the large uncertainty in low-latitude feedbacks.

The large mixing scale of the tropical response also explains why there is a single pattern that dominates the spread in the model response to a given forcing scenario, and why this pattern is highly correlated to ECS. There are multiple independent sources of uncertainty in the radiative feedbacks, i.e., multiple degrees of freedom in the $\delta\lambda_j$ vector. However, most of the uncertainty in radiative feedbacks is concentrated in the

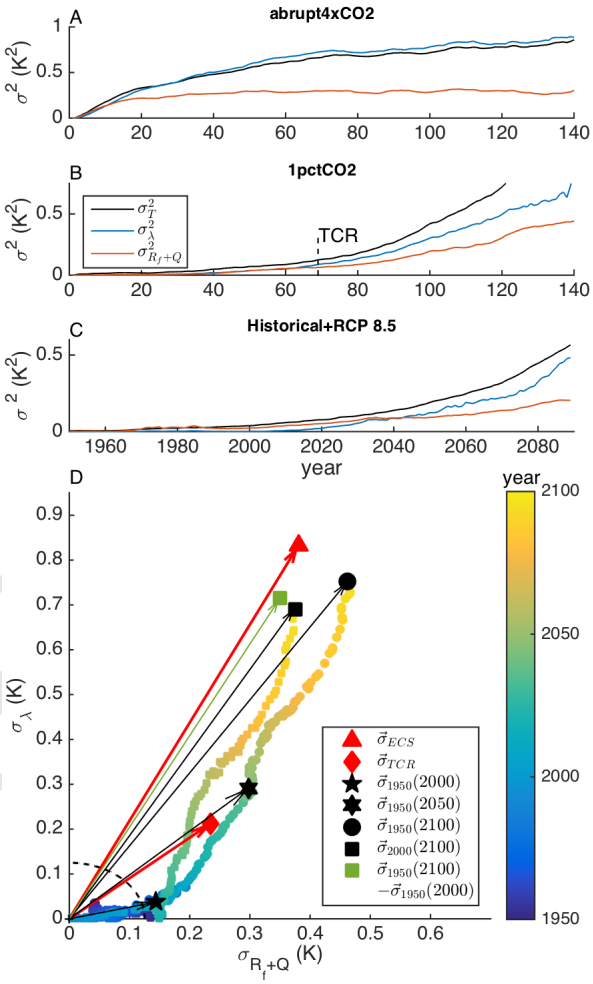

Fig. 4. Partition of uncertainty Variance of ensemble spread in global-mean temperature (black), partitioned into contributions from radiative feedbacks (blue) and radiative forcing and heat uptake (red), through multiple linear regression (Methods). (A) Abrupt4xCO2 simulations, (B) 1pctyrCO2 simulations, with dashed line marking the time TCR is evaluated, (C) historical+RCP 8.5 simulations. (D) Standard deviations of ensemble spread, partitioned into a contribution from radiative feedbacks (y-axis) and one from radiative forcing + heat uptake (x-asis). Temperature anomalies for the historical+RCP 8.5 anomalies are shown relative to both a 1880-1950 baseline (colored circles), and a 1980-2000 baseline (colored squares). Vectors indicate the partition of uncertainty for ECS (red triangle), TCR (red diamond), 21st century warming (black square), and warming at years 2000 (black pentagram), 2050 (black hexagram), and 2100 (black circle) relative to pre-industrial. The angle between two vectors gives a qualitative indication of the correlation between the ensemble spreads they represent. If the two sources of uncertainty, σ_λ and σ_{R_f+Q} were independent, than the relation between correlation and angle would be exact, and uncertainty in 21st century warming (black square) could be represented as the vector difference between uncertainties in warming relative to pre-industrial in years 2100 and 2000 (green square).

low latitudes, and the response function to low-latitude perturbations is nearly uniform on global scales (Fig. 3). Thus, the cumulative response at every latitude will be a nearly identical weighted average of the response to each low-latitude perturbation, leading to the self-similarity exhibited in Fig. 2B,E, and a high correlation between local and global temperature. Since ECS is by definition an average of the temperature response, it will be strongly correlated with local temperature change.

ECS, TCR, and the time-evolution of uncertainty

We have so far discussed the large skill of ECS in predicting both global and regional transient temperature changes over the 21st century. However, as recently noted in ref. (13), the larger skill of ECS relative to TCR is a somewhat surprising result, given that TCR was specifically designed to summarize the transient response.

To understand how it comes about, we consider how the partition of variance evolves in time. As previously noted, we do not have a way to readily diagnose regional uncertainty in radiative forcing over historical and RCP simulations for all models. However, given the large correlation between regional and global uncertainty, we can draw insight by understanding how the variance, σ_T^2, of the ensemble spread in global temperatures evolves in time. We do this by estimating the contributions to the ensemble spread in global temperature, ECS, and TCR from the spread in each model's net equilibrium radiative feedback, σ_λ^2, and the joint contribution from the spread in global-mean radiative forcing and ocean-heat uptake, $\sigma_{R_f+Q}^2$, estimated using a multiple linear regression (Fig. 4, Methods). Note that this decomposition is only an approximation, since the spread in feedbacks is not independent from the spread in radiative forcing and ocean-heat uptake, and thus the individual variances σ_λ^2 and $\sigma_{R_f+Q}^2$ will not exactly sum up to σ_T^2.

We find that the relative contribution of the uncertainty in radiative feedbacks to the uncertainty in global temperatures increases with time-scale. This can be understood from the structure of Eqn. 4, which shows that impact of uncertainty in radiative feedbacks on ensemble spread σ_T^2 is proportional to the ensemble-mean warming $\langle T \rangle$. Following an increase in radiative forcing, temperature will slowly increase, while heat uptake is a maximum immediately after the imposed forcing, declining to zero at equilibrium. As long as the growth rate of temperature is larger than the growth rate of radiative forcing, the relative importance of radiative feedbacks will increase in time. This increased relative importance of radiative-feedback uncertainty is consistent with the predictions of ref. (26) based on a simple energy balance model with separate fast and slow time scales (27).

Consistent with ref. (28), Fig. 4C shows that uncertainty in 20th century warming is dominated by uncertainty in forcing and heat uptake, whereas uncertainty in warming over the 21st century is dominated by uncertainty in radiative feedbacks. For ECS, uncertainty in radiative feedbacks contribute roughly $\sim 5-6$ times more variance than uncertainty in radiative forcing. TCR is defined as the temperature at the time of doubling (year 69) in a simulation with a 1% per year increase in CO_2, when radiative feedbacks contribute roughly the same amount of variance as radiative forcing and ocean heat uptake.

As the relative contribution of radiative feedback uncertainty increases with time, so will the correlation of warming uncertainty with ECS (Fig. 4D). For anomalies relative to a 1880-1950 baseline, the relative contributions to uncertainty will resemble the contributions to ECS more than that to TCR starting in the second part of the 21st century. This is qualitatively illustrated in Fig. 4D as the angle relative to ECS becomes smaller than the angle relative to TCR sometime between years 2050 and 2100. By rebasing the anomalies relative to a 1980-2000 baseline, we are removing the spread in temperatures predictions for the baseline 1980-2000 period. Since this removes more spread due to radiative forcing and heat uptake than due to radiative feedbacks, the uncertainty contributions to rebased temperatures will shift more towards more relative contributions from radiative feedbacks. This explains why 21st century warming trends are even more correlated with ECS than warming considered relative to pre-industrial baselines (13). This is qualitatively illustrated in Fig. 4D by the fact that temperatures relative to year 2000 tend to form a sharper angle with ECS than temperatures relative to pre-industrial conditions.

Conclusions

Uncertainty in both annual-mean and seasonal regional warming has a relatively simple structure, with a low number of degrees of freedom. Over most of the mid- and low-latitudes, and especially over land, regional uncertainty is dominated by a single pattern of uncertainty. We note that no dominant pattern of uncertainty is evident in precipitation (not shown), and that further work should also asses uncertainty in other metrics of climate change such as changes in temperature variability, extremes, and threshold-crossing events.

This single dominant pattern of regional warming arises because of the large mixing scales of atmospheric heat-transport. While the single pattern of uncertainty in temperature comes from mixing uncertainty in radiative feedbacks across a wide range of latitudes, by far the largest source of uncertainty are the equatorial and sub-tropical radiative feedbacks.

It is possible that there are sources of uncertainty that GCMs do not properly account for, which could lead to additional uncertainty in local temperatures. For example, uncertainties in land-use changes that are poorly represented in models can alter local temperature by altering the land-surface Bowen ratio (29, 30), without necessarily violating the assumption of weak MSE gradients. However, the fact that a simple, zonally-symmetric MEBM is able to capture the dominant structure and magnitude of regional temperature uncertainty in full-complexity GCM adds theoretical support to the notion that regional uncertainty is strongly dominated by large-scale energetic constraints.

Our analysis suggests that there are limits to how much we could improve regional climate projections by improving representations of regional processes. This is because even if an improved representation of regional processes were to be achieved within GCMs, the large uncertainty in regional projections coming from global-scale processes would remain.

Going forward, the greatest gain in reducing uncertainties in regional temperature predictions around the world can be obtained through improved representations of subtropical clouds processes, or through improved global constraints on ECS derived from either improved observations or from paleoclimate proxies.

Materials and Methods

GCM data. Models used reflect availability of data from Earth System Grid Federation (https://esgf-node.llnl.gov/search/cmip5/) and Center for Environmental Data Analysis (ceda.ac.uk) as of March 10, 2020. The models used for the MEBM analysis reflect the models calibrated in ref. (20). The models used for the analysis in fig. 4 reflects the models for which adjusted radiative forcing was computed along RCP8.5 in ref. (31). 25 available GCMs were used for the RCP 8.5 and RCP 4.5 ensembles and 14 available GCMs were used for the RCP6.0 and RCP2.6 ensembles. MEBM parameters are calibrated to 19 GCMs. The complete list of models used for each analysis is presented in table S1. Unless otherwise noted in Table S1, values of ECS, TCR, and the radiative forcing, $F_{2\times}$, associated with a doubling of atmospheric CO_2, are taken from ref. (32).

Partition of Regional Uncertainty. The partition of uncertainty in global temperature for purposes of Fig. 2A-C is computed using temperature anomalies from an ensemble of 19 RCP8.5 simulations for which zonal-mean radiative feedbacks have been previously diagnosed in ref. (20). We compute point-wise squared cross-correlation r^2 of ensemble spread in zonal-mean 21$^{\text{st}}$ century warming in RCP8.5 simulations with ensemble spread in model ECS, zonal-mean 21$^{\text{st}}$ surface heat uptake, and the zonal-mean radiative feedbacks from ref. (20).

MEBM. Radiative forcing and feedbacks cannot be diagnosed from available RCP8.5 and 1pctCO2 simulations. Hence we use MEBM parameters (radiative feedbacks, λ, radiative forcing per CO_2 doubling, R_f) and ocean heat uptake patterns calibrated to an abrupt quadrupling simulation ref. (20). To maximize the ability of the MEBM to replicate the CMIP5 ensemble, we set the diffusion coefficient to D_0=1.35 W/m^2/K per (12). A latitude grid of 101 points is used with a constant $\Delta x = \Delta(\sin\phi)$ in order to create an equal-area grid.

The ECS for the MEBM is computed by integrating the MEBM with heat fluxes set to zero. TCR is defined as the global temperature response at the time of doubling in an experiment where CO_2 is increasing at 1% per year. To compute the MEBM TCR we set the effective radiative forcing to half of the value diagnosed from the abrupt quadrupling experiments. We also keep the same patterns of heat uptake, but rescale them by the ratio of global-mean heat uptake in the ensemble mean 1pctCO2 experiment at doubling relative to heat uptake in 2090 in an RCP8.5 simulation, using 20-year windows.

The MEBM response function, $\partial T_i/\partial F_j$ is computed by perturbing the radiative forcing term R_f using Gaussian perturbations, $\delta R_f(\phi_i) \propto \exp[-(x_i - x_j)/w^2]$, centered at 40 equidistant latitudes, $\phi_j = \text{asin}(x_0)$, and normalized to unit net radiative forcing of $\sum R_f(\phi_i) = 1\text{W/m}^2$. The response function for perturbations at other locations is interpolated from the 40 gaussian bump integrations. The response function presented in Fig. 3A is computed for each calibration of the MEBM to a GCM, then averaged across the ensemble.

Partition of Global Uncertainty. The partition of uncertainty in global temperature for purposes of Fig. 4 is computed using temperature anomalies from an ensemble of 18 GCMs. For RCP scenarios, the spread in temperature projections $\delta T(t)$ is regressed simultaneously against the equilibrium radiative feedback, radiative forcing, and heat uptake,

$$\delta T(t) = \beta_\lambda(t) \cdot \delta\lambda + \beta_{Rf}(t) \cdot \delta R_f(t) + \beta_Q(t) \cdot \delta Q(t) + \text{error}. \quad [5]$$

The regression is done every year, using a 20 year averaging window. The global equilibrium radiative feedbacks, λ, are computed as $\lambda = F_{2\times}/\text{ECS}$. For ECS and TCR, the spread in radiative forcing comes from the spread in $F_{2\times}$. For the historical+RCP8.5 ensembles, the spread in adjusted radiative forcing, R_f, is taken from ref. (31). For all simulations, net heat uptake is computed as the net imbalance at the top of the atmosphere. The variance due to radiative feedbacks, $\sigma^2_\lambda(t)$ is computed as the standard deviation of $\hat{\beta}_\lambda(t) \cdot \delta\lambda$, while the variance due to radiative forcing $\sigma^2_\lambda(t)$ and heat uptake is computed as the the standard deviation of $\hat{\beta}_{Rf}(t) \cdot \delta R_f(t) + \hat{\beta}_Q(t) \cdot \delta Q(t)$. $\hat{\beta}_j(t)$ denotes the least-squares estimate of the regression coefficients.

ACKNOWLEDGMENTS. CP was supported by a JISAO postdoctoral fellowship, the National Science Foundation (award number AGS-1752796) and the Tamaki foundation. DSB was supported by a gift from the Tamaki foundation. KCA was supported by the National Science Foundation (award number AGS-1752796). We thank Nick Lutsko for constructive comments.

1. F Lehner, TF Stocker, From local perception to global perspective. *Nat. Clim. Chang.* **5**, 731 (2015).
2. SI Seneviratne, MG Donat, AJ Pitman, R Knutti, RL Wilby, Allowable CO_2 emissions based on regional and impact-related climate targets. *Nature* **529**, 477 (2016).
3. E Hawkins, R Sutton, The potential to narrow uncertainty in regional climate predictions. *Bull. Am. Meteorol. Soc.* **90**, 1095–1108 (2009).
4. R Knutti, J Sedláček, Robustness and uncertainties in the new CMIP5 climate model projections. *Nat. Clim. Chang.* **3**, 369 (2013).
5. S Manabe, RJ Stouffer, Sensitivity of a global climate model to an increase of CO_2 concentration in the atmosphere. *J. Geophys. Res. Ocean.* **85**, 5529–5554 (1980).
6. R Stouffer, S Manabe, K Bryan, Interhemispheric asymmetry in climate response to a gradual increase of atmospheric CO_2. *Nature* **342**, 660 (1989).
7. E Hawkins, R Sutton, The potential to narrow uncertainty in projections of regional precipitation change. *Clim. Dyn.* **37**, 407–418 (2011).
8. T Stocker, *Climate change 2013: the physical science basis: Working Group I contribution to the Fifth assessment report of the Intergovernmental Panel on Climate Change.* (Cambridge University Press), (2014).
9. F Pithan, T Mauritsen, Arctic amplification dominated by temperature feedbacks in contemporary climate models. *Nat. Geosci.* **7**, 181 (2014).
10. MF Stuecker, et al., Polar amplification dominated by local forcing and feedbacks. *Nat. Clim. Chang.* **8**, 1076 (2018).
11. MP Byrne, PA O'Gorman, Trends in continental temperature and humidity directly linked to ocean warming. *Proc. Natl. Acad. Sci.* **115**, 4863–4868 (2018).
12. KC Armour, N Siler, A Donohoe, GH Roe, Meridional atmospheric heat transport constrained by energetics and mediated by large-scale diffusion. *J. Clim.* **32**, 3655–3680 (2019).
13. MR Grose, J Gregory, R Colman, T Andrews, What climate sensitivity index is most useful for projections? *Geophys. Res. Lett.* **45**, 1559–1566 (2018).
14. KE Taylor, RJ Stouffer, GA Meehl, An overview of CMIP5 and the experiment design. *Bull. Am. Meteorol. Soc.* **93**, 485–498 (2012).
15. R Moss, et al., Towards new scenarios for the analysis of emissions: Climate change, impacts and response strategies (2008).
16. BD Santer, TM Wigley, ME Schlesinger, JF Mitchell, *Developing climate scenarios from equilibrium GCM results.* (Max-Planck-Institut für Meteorologie), (1990).
17. N Herger, BM Sanderson, R Knutti, Improved pattern scaling approaches for the use in climate impact studies. *Geophys. Res. Lett.* **42**, 3486–3494 (2015).
18. TD Mitchell, Pattern scaling: an examination of the accuracy of the technique for describing future climates. *Clim. change* **60**, 217–242 (2003).
19. C Tebaldi, JM Arblaster, Pattern scaling: Its strengths and limitations, and an update on the latest model simulations. *Clim. Chang.* **122**, 459–471 (2014).
20. D Bonan, K Armour, G Roe, N Siler, N Feldl, Sources of uncertainty in the meridional pattern of climate change. *Geophys. Res. Lett.* **45**, 9131–9140 (2018).
21. PM Caldwell, MD Zelinka, KE Taylor, K Marvel, Quantifying the sources of intermodel spread in equilibrium climate sensitivity. *J. Clim.* **29**, 513–524 (2016).
22. BP Flannery, Energy balance models incorporating transport of thermal and latent energy. *J. Atmospheric Sci.* **41**, 414–421 (1984).
23. YT Hwang, DM Frierson, Increasing atmospheric poleward energy transport with global warming. *Geophys. Res. Lett.* **37** (2010).
24. BE Rose, KC Armour, DS Battisti, N Feldl, DD Koll, The dependence of transient climate sensitivity and radiative feedbacks on the spatial pattern of ocean heat uptake. *Geophys. Res. Lett.* **41**, 1071–1078 (2014).
25. GH Roe, N Feldl, KC Armour, YT Hwang, DM Frierson, The remote impacts of climate feedbacks on regional climate predictability. *Nat. Geosci.* **8**, 135 (2015).
26. NJ Lutsko, M Popp, Probing the sources of uncertainty in transient warming on different timescales. *Geophys. Res. Lett.* **43** (2019).
27. IM Held, et al., Probing the fast and slow components of global warming by returning abruptly to preindustrial forcing. *J. Clim.* **23**, 2418–2427 (2010).
28. JA Crook, PM Forster, A balance between radiative forcing and climate feedback in the modeled 20th century temperature response. *J. Geophys. Res. Atmospheres* **116** (2011).
29. SI Seneviratne, et al., Investigating soil moisture–climate interactions in a changing climate: A review. *Earth-Science Rev.* **99**, 125–161 (2010).
30. ND Mueller, et al., Cooling of us midwest summer temperature extremes from cropland intensification. *Nat. Clim. Chang.* **6**, 317–322 (2016).
31. PM Forster, et al., Evaluating adjusted forcing and model spread for historical and future scenarios in the CMIP5 generation of climate models. *J. Geophys. Res.: Atmos.* **118**, 1139–1150 (2013).
32. G Flato, et al., Evaluation of climate models in *Climate change 2013: the physical science basis. Contribution of Working Group I to the Fifth Assessment Report of the Intergovernmental Panel on Climate Change.* (Cambridge University Press), pp. 741–866 (2014).